Hack, E., Fruehmann, R.K., Roos, R., Feligiotti, M., Schuetz, P., Tyler, J.P. and Dulieu-Barton, "Flaw and damage assessment in torsionally loaded CFRP cylinders using experimental and numerical methods", Composite Structures, 132, 2015, 109-121. doi:10.1016/j.compstruct.2015.05.025

Flaw and damage assessment in torsionally loaded CFRP cylinders using experimental and numerical methods

Erwin Hack[a*], Richard K. Fruehmann[b], René Roos[c], Mara Feligiotti[a], Philipp Schuetz[a], John P. Tyler[d] and Janice M. Dulieu-Barton[b]

[a] * Empa, Reliability Science and Technology Laboratory, 8600 Dubendorf, Switzerland, erwin.hack@empa.ch

[b] University of Southampton, Faculty of Engineering and the Environment, Southampton, UK , janice@soton.ac.uk

[c] ANSYS Switzerland GmbH, Technoparkstrasse 1, 8005 Zurich, Switzerland, rene.roos@ansys.com

[d] Enabling Process Technologies Ltd., Bristol, BS208ET, UK, philip.tyler@eptworld.com

Abstract

CFRP structural elements are prone to failure initiating from defects. While defects are expected after damage has occurred, flaws and voids can already be present after manufacturing. To study the criticality of such defects CFRP cylinders have been manufactured from a lay-up that was designed to predict damage mode and to allow for controlled damage growth under torsional load. FEA simulations of defect-free and flawed cylinder models were performed to first ply / interface failure. X-ray Computed Tomography revealed that cylinders manufactured with different finishing had a completely different void content and distribution. Simulations of failure, using finite element models, for the two classes of void distribution are corroborated by experimental results for the ultimate load, and damage initiation from manufacturing flaws is confirmed. Digital Speckle Pattern Interferometry was used to identify flaws using thermal and mechanical loading, while infrared thermography and thermoelastic stress analysis were used to identify possible failure initiation sites and monitor the failure process and damage growth, whilst the specimen was loaded in torsion.

Keywords: A. Carbon fibre; B. Defects; C. Finite element analysis (FEA); D. Non-destructive testing

* Corresponding author, erwin.hack@empa.ch

Abbreviations

ACP	ANSYS Composite PrepPost 14.5
CFRP	Carbon Fibre Reinforced Polymers
CT	Computed Tomography
DSPI	Digital Speckle Pattern Interferometry
FEA	Finite element analysis
FRP	Fibre Reinforced Polymers
IRF	Inverse Reserve Factor
IRT	infrared thermography
MATERA+	ERA-NET Plus on Materials Research
pd	Puck ply delamination
pmA	Puck matrix failure mode A
pmB	Puck matrix failure mode B
pmC	Puck matrix failure mode C
TSA	Thermoelastic stress analysis
UD	uni-directional
WB	ANSYS Workbench 14.5

Hack, E., Fruehmann, R.K., Roos, R., Feligiotti, M., Schuetz, P., Tyler, J.P. and Dulieu-Barton, "Flaw and damage assessment in torsionally loaded CFRP cylinders using experimental and numerical methods", Composite Structures, 132, 2015, 109-121. doi:10.1016/j.compstruct.2015.05.025

1. Introduction

The design and manufacture of a structural element is normally followed by specific tests up to and beyond operational loads to qualify the product in view of potential material variability. As CFRP structural elements are prone to failure initiating from defects, an assessment of manufacturing quality, monitoring at regular intervals, as well as a re-assessment after an incident is recommended [1]. A major challenge remains in estimating the expected residual life of a component after detection of damage. While in fortuitous or well controlled experiments damage in CFRP can evolve gradually, in most service cases damage grows in an unpredictable manner leading to catastrophic failure. It is therefore of utmost importance to understand the failure initiators and link the damage growth to the degrading at a structural scale, e.g. by relating the damage type, size and location to the effect on the strain fields developed under operating load.

A recently completed European MATERA+ project [2] was aimed at assessing the performance of composite structures, by both the detection of defects and providing an estimation of their effect on the residual strength and/or lifetime. The present paper describes a part of the project that examined the use of simulations alongside experimental examinations of defective CFRP components. The experiments informed a *Finite Element Analysis* (FEA) of the components so that defects could be included. Thus providing an improved estimation of failure through re-simulation, with a view to developing a basis for making decisions on retaining, repairing or replacing the component.

The criticality of defects in FRP components has been studied with a general aim to determine the failure modes of the material and hence inform remaining life of components or structures [3]. The approach is to generate defined individual failure modes and use these to assess their criticality on an overall structure. A different approach would be to introduce artificial defects to simulate debonds, e.g. using Teflon inserts [4, 5] or resin inclusions [6]. However these rarely generate realistic structural failure modes. When multi-axial or combined mechanical loading is essential, it is common practice to use cylindrical components. It was shown that loading a cylinder in torsion provided a more realistic structure than plain coupons of material, e.g. for fatigue loading [7]. Some examples of using cylinders for multiaxial load testing exist in the literature, e.g. [8, 9].

In the present paper, a CFRP cylinder was designed with a lay-up that encourages a controlled damage initiation and evolution whilst under torsional loading. The proposed outcome was to generate a known

failure type, viz. a delamination, and to study failure initiation and damage propagation under defined conditions. The paper describes the specimen design, the experimental methodologies and their combination with numerical modelling. From the actual failure modes and their relation to the type of manufacturing flaws the numerical model was updated to reproduce the experimental outcome.

2. Test specimen

2.1 Designing failure mode

Torsional loading of CFRP cylinders induces shear stresses which, depending on the fibre orientation and lay-up, are transformed into matrix shear and/or matrix and fibre compression and tension stresses. Based on the description of failure modes in cylinders loaded in torsion by Puck [10], three different matrix failure modes are predicted, depending on the layup and the loading direction, two of which dominate in ±45° layers: mode A (tensile matrix failure pmA) and mode C (compressive matrix failure pmC). Mode C leads to a 50° through thickness fracture surface, as exemplified in Figure 1 for the simplest two-layer model. The fracture surface presents a slip plane from which delamination stresses result. By varying the layup, it is possible to tailor the cylinder to fail in a particular mode [11]. The CFRP cylinders in this work were designed with a lay-up (inside to outside) of $[0°]_3$ $[-45^o]_{14}$ $[+45^o]_6$ with respect to the cylinder longitudinal axis. Finite element analysis (FEA) was used to assess this layup under torsional loading. The FEA (described in detail in section 2.2) predicted initial matrix compression failure pmC in the -45° plies, when loading in torsion so that the fibres in the external +45° layer are in compression. This initial pmC failure then would lead to a progressive delamination in the ±45° interface which was enforced by adding the three 0° layers at the inside of the cylinder.

Using the corresponding material parameters, the predicted torsional failure load was 5900 Nm. This mode of failure was designed into the specimen to promote a gradual failure in contrast to a sudden catastrophic failure as would occur e.g. in a fibre failure scenario. It should be noted for this laminate configuration that the failure load is independent of the direction of torsion, but the failure mode will change if the loading direction is reversed, i.e. if the outer fibres are loaded in tension, fibre failure will occur in the outer layer, Figure 1. For a representative model failure prediction should be accurate to within ±10 % of an experiment [12].

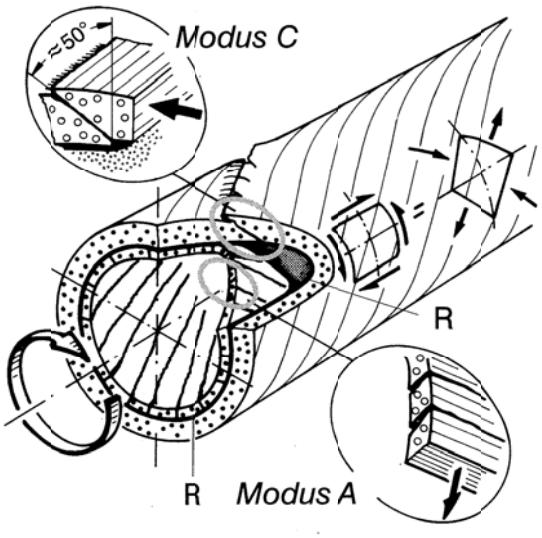

Figure 1: Puck matrix failures (reproduced from [10]).

2.2 Manufacturing

The cylinders were fabricated using 150 g/m^2 UTS50 F24 24K 1600tex D fibres from Toho Tenax and 90 g/m^2 resin Huntsman XB 3515/Aradur 5021 BD, 37.5 wt%. The ply thickness is 0.16 mm, the fibre volume content is 52.1% and the density of the prepreg is 1490 kg/m^3. The cylinders had a length of 500 mm, an inner diameter of 55 mm, and a total wall thickness of 3.6 mm. Two types of cylinders with the same lay-up but different finishing were studied, see Figure 2. Two samples were manufactured with a smooth finish (specimens B0 and B1) while other samples (#B2 – B6) were tightly wrapped with peel ply tape before cure, resulting in a rough surface finish when the peel ply was removed. Steel inserts with square ends to fit the test machine were bonded into the cylinder ends using 3M Scotch-Weld 9323 B/A.

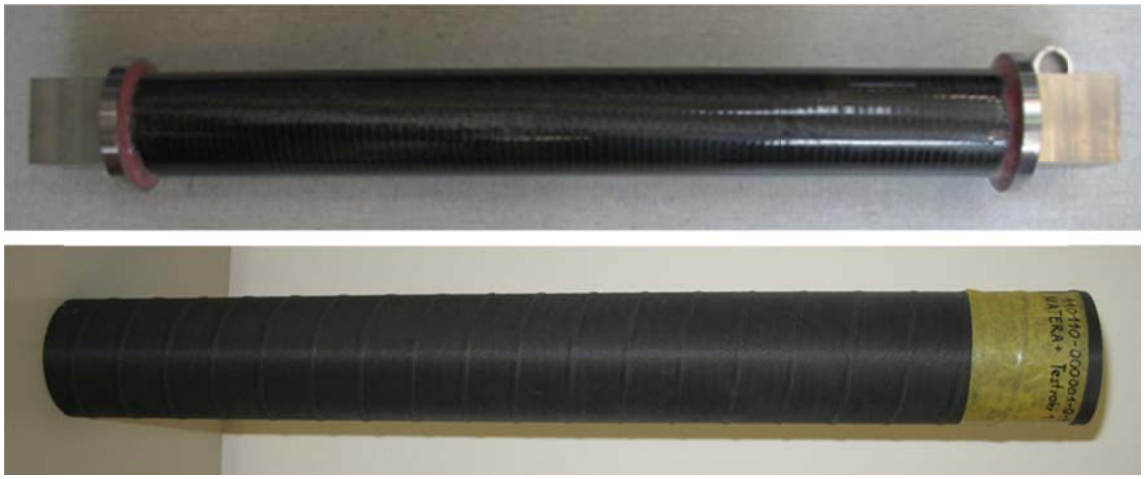

Figure 2: Test sample B1 as manufactured with steel inserts for torsion testing (top), and sample B6 with peel ply finish (bottom).

2.3 Finite Element Analysis

ANSYS Workbench 14.5 (WB) and ANSYS Composite PrepPost 14.5 (ACP) were used for the finite element analysis (FEA). The material properties of structural steel (used to model the metallic inserts) and of the carbon prepreg (used to model the cylinder) are listed in Table 1. The material properties of the carbon prepreg were derived from the raw materials using rules of mixtures and unpublished data gained from mechanical tests of similar materials. The raw materials and resin weight content are given in Section 2.2 above. The orthotropic elasticity and stress limits as well as the Puck constants for carbon UD prepreg are listed in Table 1.

An initial cylinder model was generated using WB. The steel inserts were meshed with quadratic tetra elements (solid187), while the cylinder was meshed with quadratic shell elements (shell281). The inner cylinder surface generated in WB was used as a reference surface in ACP to define the laminate and to generate a layered solid model (solid186) which included all laminate information and orthotropic material definitions. The solid cylinder had 23 elements through the thickness (one for each layer). This full solid model allows capturing 3D effects such as out-of-plane and interface stresses that cannot be studied using layered shell elements. The element dimensions in the central portion of the cylinder were 4 x 4mm (l_{axial} x w_{radial}). The fibre orientation of the 0, –45° and +45° layer with respect to the global coordinate system is shown in Figure 3.

In the model assembly, the steel inserts and solid carbon cylinder are joined together through a bonded contact, Figure 4. Stress concentrations were anticipated at the interface between the steel inserts and the carbon fibre cylinder. Mesh refinement at these locations was performed until sufficient stress convergence (< 1% change in predicted stress) was reached. In analogy to the test machine, the loading is applied to the lateral faces of the metallic inserts highlighted in blue and red in Figure 4. The fixed support is defined on the left and the positive torsional moment is applied through a deformable remote point on the right. The axis of the torsional moment is aligned with the global x-axis. The red arrow on the right indicates the orientation of the torsional moment. Torsion with this orientation applies a compressive load to the fibres of the outer +45° layers and a tensile load to the inner –45° layers.

Table 1: Material property values of the steel inserts and the carbon unidirectional (UD) prepreg used in the FEA. Parameter definitions are found in ref [13].

Structural Steel	E = 200.0 GPa ν= 0.30		
Carbon UD prepreg	Orthotropic Elasticity		
	E_1 = 123.34 GPa	ν_{12} = 0.27	G_{12} = 5.00 GPa
	E_2 = 7.78 GPa	ν_{13} = 0.27	G_{13} = 5.00 GPa
	E_3 = 7.78 GPa	ν_{23} = 0.42	G_{23} = 3.08 GPa
	Orthotropic Stress Limits [MPa] [1]		
	X_T = 2600	Y_T = 34	Z_T = 34
	X_C = -1300	Y_C = -68	Z_C = -68
	S_{12} = 80	S_{13} = 80	S_{23} = 55
	Puck Constants [dimensionless]		
	$p_{\perp\parallel}^{(+)}$ = 0.35	$p_{\perp\parallel}^{(-)}$ = 0.30	
	$p_{\perp\perp}^{(+)}$ = 0.30	$p_{\perp\perp}^{(-)}$ = 0.25	
	Degradation factor M = 0.5	Degradation factor s = η = 0.5	Interface weakening factor f_w = 0.8

[1] **For unidirectional prepreg, X and Y correspond to the failure stresses in the principal material directions (i.e. 1 and 2). S is the failure shear stress. The subscripts T and C stand for tension and compression, respectively.**

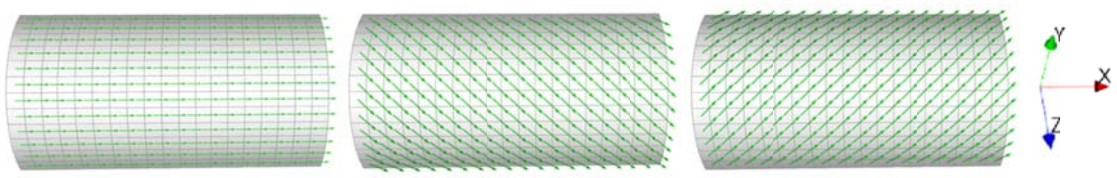

Figure 3: Fibre orientation for 0°, –45°, +45° and the global coordinate system.

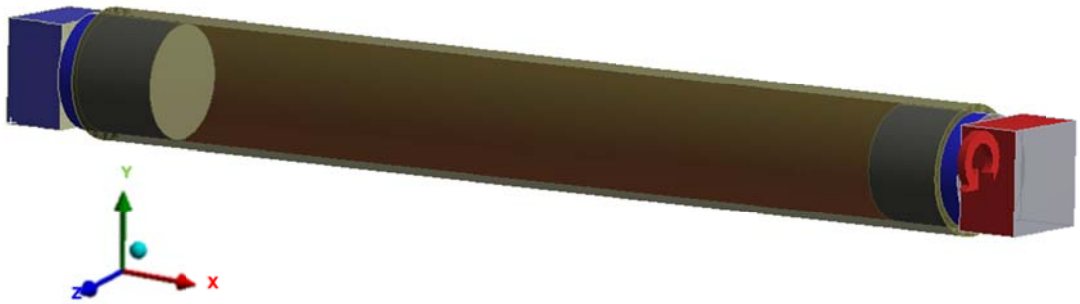

Figure 4: Model assembly - bonded contact of the steel inserts and CFRP cylinder. Boundary conditions: fixed support on the left and torsional moment is applied on the right.

3. Test methods and procedures

Pre-assessment of the pristine cylinders was carried out using DSPI and X-ray CT to identify manufacturing flaws and damage and, during loading, using IRT and TSA to identify failure initiation sites and the change of stress distribution as the damage evolves. Table 2 summarizes the specimens, the torsion tests and the type of measurement.

Table 2: Test specimens, surface finish, torsion tests and measurements performed.

No	Finish	Torsion tests	IRT	TSA	DSPI	CT scan
B0	smooth	Quasi-static load to 1000 Nm	-	-	post failure	-
B1	smooth	Quasi-static load to 1200 Nm Cyclic load, defect grown by fatigue cycling	-	pristine and after defect growth	pristine and after defect growth	pristine
B2	peel-ply	fatigued to 80000 cycles Quasi-static test to failure 1400 Nm	during failure event	Every 1500 cycles	pristine	-
B3	peel-ply	Quasi-static test to failure 1300 Nm	during failure event	pristine	post failure	post failure
B4	peel-ply	Quasi-static test to failure 1400 Nm	during failure event	pristine	pristine	-
B5	peel-ply	Quasi-static test to failure	during	pristine	pristine	-

		1500 Nm	failure event			
B6	peel-ply	not loaded	-	-	pristine	pristine

3.1 X-ray CT inspection

X-ray CT scans of cylinders with both finishing types were performed on representative sections to identify size and distribution of manufacturing flaws [14]. The cylinders were scanned with an X-ray cone-beam micro-tomography setup consisting of an X-ray tube "XT9160-TXD" from Viscom with a focal spot of 4 µm at an acceleration voltage of 80 kV and 120-125 µA tube current, a rotation table "UPR-160F air" from Micos and an X-ray flat panel detector "1621-CN3 ES" from Perkin Elmer. For all CT measurements an exposure time of 3.6 s was chosen. The projection images were reconstructed with an in-house GPU implementation of the Feldkamp-David-Kress algorithm [15]. For sample B1, a total of 720 projections were recorded yielding a volume of 1400 x 1400 x 2048 voxels with a nominal size of 50x50 x50 μm^3. In the measurement of sample B3, 720 projections were used to reconstruct a volume of 1200 x 1200 x 2000 voxels with a nominal size of 60 x 60 x 60 μm^3. A total of 900 projections were acquired from sample B6 to reconstruct a volume of 1400 x 1400 x 2048 voxels with a nominal size of 50 x 50 x 50 μm^3. The data were analysed with the commercial software package VG Studio Max 2.2 from Volume Graphics (Heidelberg, Germany). The Defect Analysis Module was used to calculate the defect size, while the Wall Thickness Module was used to calculate the defect depth.

3.2 DSPI inspection

DSPI was performed in the laboratory over the entire specimen surface to find and delineate flaws. Phase maps for in- and out-of-plane deformation were obtained using a 3D DSPI set-up (Steinbichler Optotechnik GmbH, Neubeuern, Germany), from which phase gradient maps were obtained to better visualize damage size. Loading of the cylinders was by halogen lamp heating from outside, hot air from inside, or by mechanical point load from the back side.

3.3 IRT and TSA inspection

TSA was used in a non-destructive cyclic loading regime to identify manufacturing flaws and to delineate defects post-failure. Assessment of the surface stresses allowed potential damage initiation sites to be

identified in the pristine specimen and to estimate the extent of damage in the damaged specimen. In addition, IRT was applied to monitor the surface temperature during quasi-static tests to failure with a view to identifying the actual failure initiation site by observing the temperature rise associated with the formation of a crack. A FLIR SC7000 series camera (FLIR Systems ATS, Croissy-Beaubourg, France) was used, with a 320 x 256 pixel Indium Antimonide detector array and a 50 mm lens. To enable the full specimen surface to be viewed simultaneously, two metallic mirrors were placed behind the specimen under an angle, see Figure 5. To obtain data with higher spatial resolution, the camera was moved closer to the specimen. To access the full specimen surface in this case, the specimen was rotated four times about 90° in the grips, and the camera was positioned at different heights to collect data along the full length of the specimen. The TSA data were then stitched together.

Figure 5: Test specimen mounted on the test machine with the two metal mirrors. Rotated view.

3.4 Torsion testing

A servo-hydraulic test machine Instron 1346 (Instron, Norwood, MA, USA) with a maximum torsional load of 20 kNm was used. The load was applied using position control. Quasi-static tests to failure were performed using an angle control ramp corresponding to about 2 Nm/s; cyclic loading with position control was applied for the TSA measurements with frequencies from 1 to 5 Hz and amplitudes in the range of 100 to 350 Nm.

4. Results

4.1 Specimen pre-assessment

X-Ray CT scans were performed on specimen B1 (smooth surface) and B6 (peel ply surface) in their pristine state. The void content and distribution differ drastically between the two types of finishing as shown in Figure 6. It can be seen that voids, up to 100 mm^3, are distributed throughout specimen B1. By contrast, the much smaller voids in B6 are concentrated in a spiral pattern coincident with the edges of the peel ply tape wrapped around the laminate during manufacturing. This indicates that the peel ply has served to 'squeeze out' a fair portion of the voids, leaving void concentrations at the peel ply overlaps. In the following, the void distribution found in specimens with smooth surface finishing is referred to as VD1, while the distribution found in specimens with peel-ply finishing is named VD2.

The histogram of the void content by size is shown in Figure 7. VD1 has fewer of the very small voids (< 0.11 mm^3) but many more in total (approximately 3 times as many) and much larger void than VD2s. This significant difference in void content would suggest a likely very large difference in ultimate strength of the component.

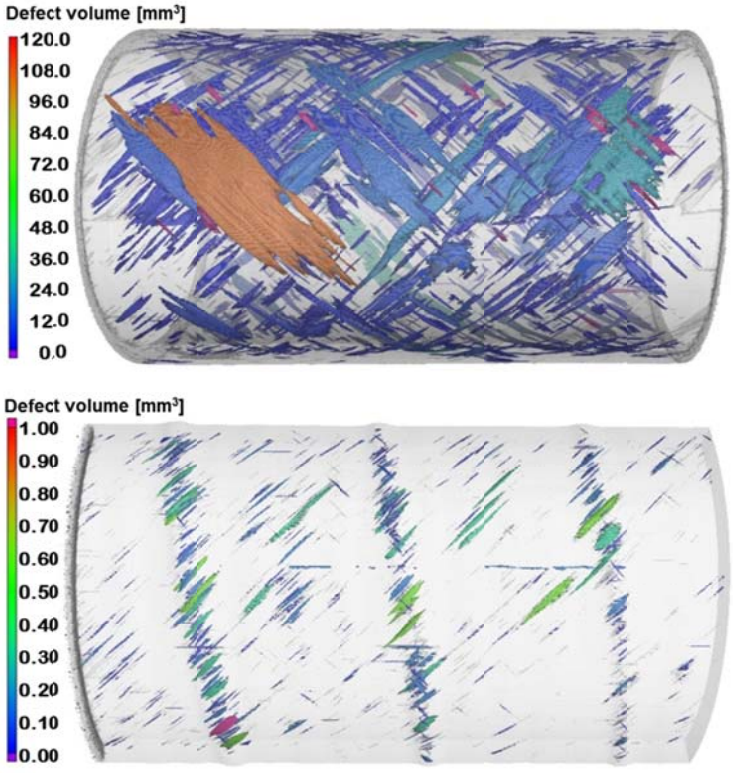

Figure 6: CT scans of a 110 mm section of cylinder B1 (top) and B6 (bottom) with colour coded defect volume. Note that the colour scale is different by a factor of 120 for the two specimens.

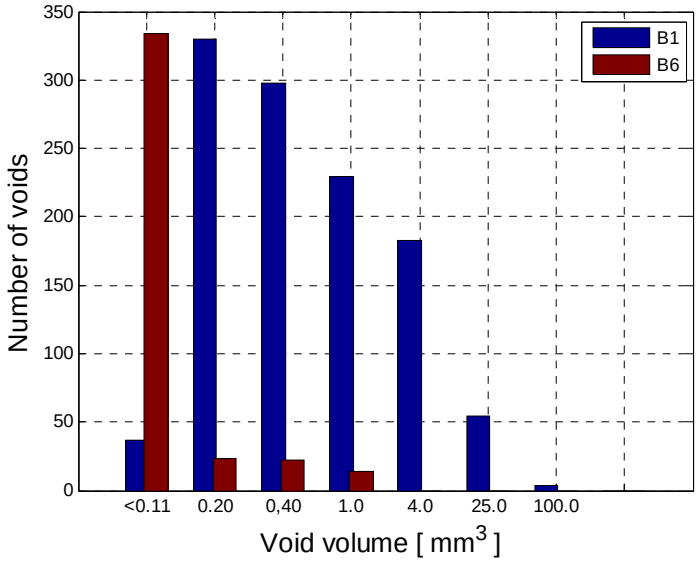

Figure 7: Void volume distribution of cylinder B1 (VD1, blue) and B6 (VD2, red).

Figure 8 shows the manufacturing flaws in cylinder B1. The map of defect depths in colour code from the CT data shows that in VD1 large defects are predominantly found in the external layers with a preferred orientation along the fibres above the void at +45°, while with increasing depth the defect volume decreases and the orientation rotates by 90°. When comparing X-ray CT scan and DSPI results obtained from the same section, it is clear that DSPI is more sensitive to the superficial voids than to voids at deeper layers. The defects were further analysed using TSA at a torsional load of 250 ±100 Nm at 5 Hz in the test machine. Again, areas with stress concentrations are seen at the same locations and confirm the results found in the CT scan. Thus, the larger defects near the surface clearly show in all three data sets (X-ray CT, DSPI and TSA). In view of the large number of voids, a one-to-one identification is neither viable nor useful for this specimen.

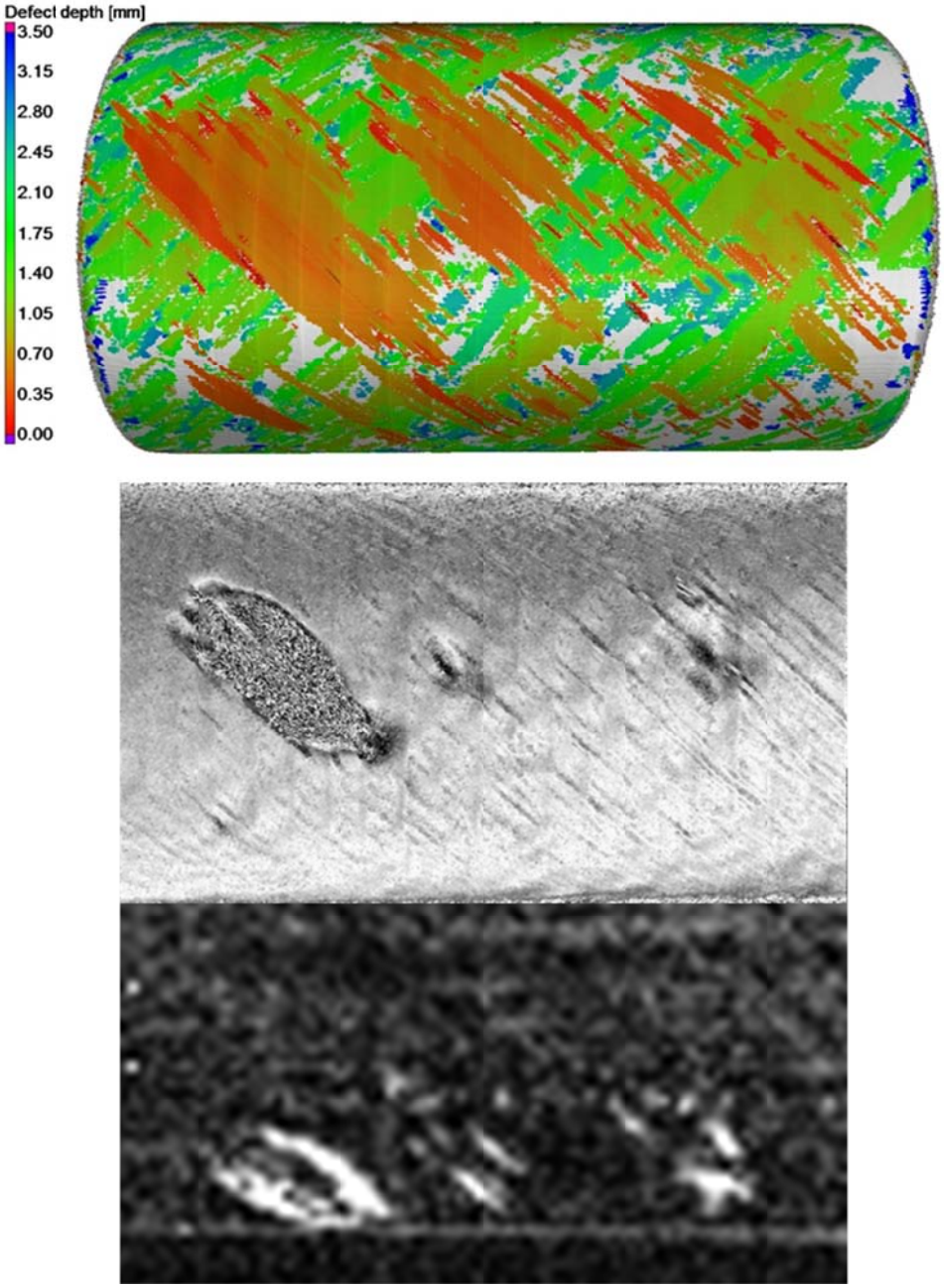

Figure 8: Section of cylinder B1 with manufacturing flaws. CT-data colour coded for defect depth (top); DSPI phase gradient data (centre). TSA amplitude data with a slightly rotated view (bottom). The images are flipped in order to reproduce the orientation of the CT data.

4.2 Refined FEA simulations

The results of the pre-assessment highlight a relevant number of initial defects which must be incorporated in the updated FE model to re-evaluate cylinder stiffness, the limit load and initial failure mode. The X-ray CT scans provided information about number, dimension, orientation and shape of the voids as well as their through-the-thickness distribution. This information was embedded into the FE

model. Again ANSYS WB-ACP was used to set up the modified FE model. ACP has the ability to specify the layup and local patches, used in this case to define voids. In addition, ACP is able to generate layered solid models based on the layup definitions. The result is a 3D (solid) FE model which provides more accurate results than a shell model, especially if out-of-plane effects have to be considered. Python scripts were used to generate the final ACP models.

To save computation costs, voids were introduced into a trimmed model, using the defect free model to provide the load boundary conditions. The voids in the model were distributed randomly according to the statistics of VD1 or VD2 extracted from the X-ray CT scans. While the orientation of the void is parallel to the fibre orientation of the ply above the void, the void shape is approximated with ellipses. Figure 9 shows two example distributions of voids representing the smooth (VD1) and rough (VD2) cylinders. The resulting solid model contained one solid element through-the-thickness for each layer as shown in Figure 10. Two voids are highlighted in green, each of which is modelled as a single additional layer with very low stiffness (air). Since the voids in distribution VD2 are much smaller compared to VD1, the element size (edge length) was reduced from 1.5 to 0.7 mm.

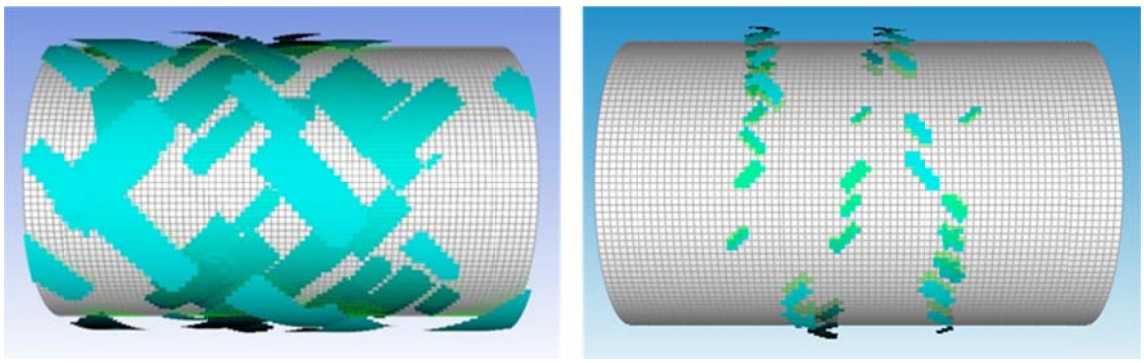

Figure 9: Exemplary void distribution for VD1 (left) and VD2 (right).

In the first step, the stiffness of cylinders with and without voids was compared. For a void volume content of 0.5% the compliance of both VD1 and VD2 turned out to be equal within 1%. Additionally, the compliance between the mechanical tests and the FE model was compared. According to the torsion test machine's angle control, the rotation around the cylinder axis at 1000 Nm was 2.32° whereas the corresponding FE result was 2.40°. This is a difference of 3.3% only.

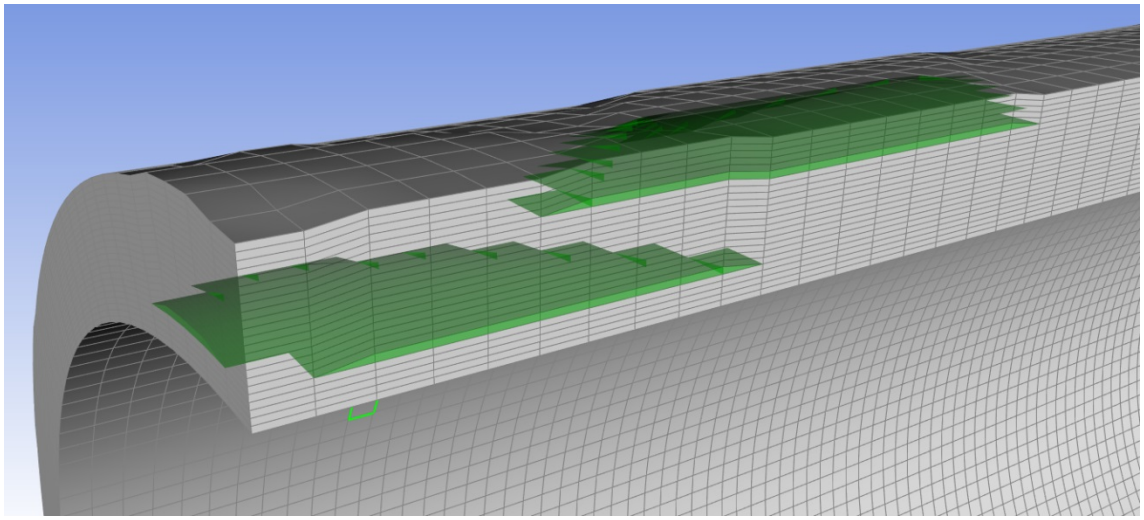

Figure 10: Section cut of the final solid model with two highlighted voids.

4.3 Effect of voids on failure strength and failure modes

The expected failure mode was calculated from the stress values reached in each laminate layer for a torsionally loaded cylinder without voids. Figure 11 shows a plot of the resulting inverse reserve factor (IRF) for each ply through the thickness of the cylinder wall, from the inner ply (left) to the outer ply (right). The IRF is the ratio of the actual load and the failure load such that a value of IRF < 1 indicates a 'safe' load, while an IRF > 1 indicates that the local stress combinations exceed the respective Puck failure criterion. For the defect free cylinder, the strength distribution is roughly homogeneous and an exemplary through-the-thickness plot shows that the maximum IRF occurs just below the –45°/45° interface highlighted with a dash-dotted line. With the external load applied such that the surface fibres are in compression, the failure mode in this and the adjacent –45° plies is shear compression (pmC) . In a cylinder without voids, it would be expected that the failure initiates in the -45° ply, just below this interface.

The effect of the voids on the failure mode was investigated by considering 50 randomly generated defect configurations based on the void distribution VD1, with the cylinder strength evaluated for each; all of the configurations gave similar results. The failure torque of the cylinders was reduced from 5900 Nm for a void-free cylinder, to 1200 Nm for a typical defect rich cylinder. A representative example of the overall failure distribution is visualized in Figure 12 in terms of the IRF. The difference between the defect free regions and those with voids is clearly identified. Furthermore the illustration shows that the orientation

of the voids has a relevant effect regarding the strength. Because orientation is given by fibre direction of the ply above the void, the voids oriented from bottom-left to top-right are found in the outer +45° layers and are prone to failure while those with a void rotated by 90° are found in the inner -45° layers and are more stable. Note that the calculated IRF at the edges of the voids are strongly influenced by edge effects resulting from the mesh. Results are therefore only to be trusted from the middle of the voids.

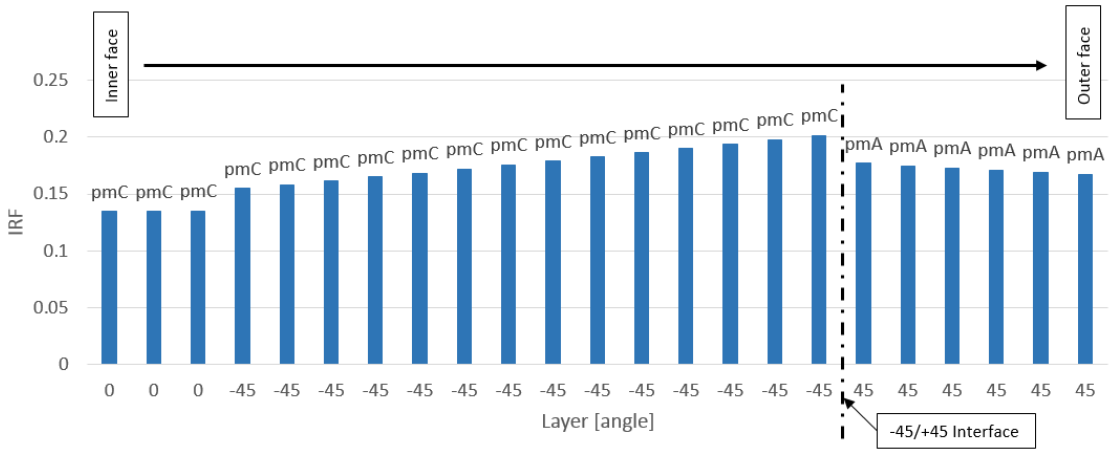

Figure 11: Inverse reserve factors for each layer of a laminate without voids calculated for a torsional moment of 1200 Nm.

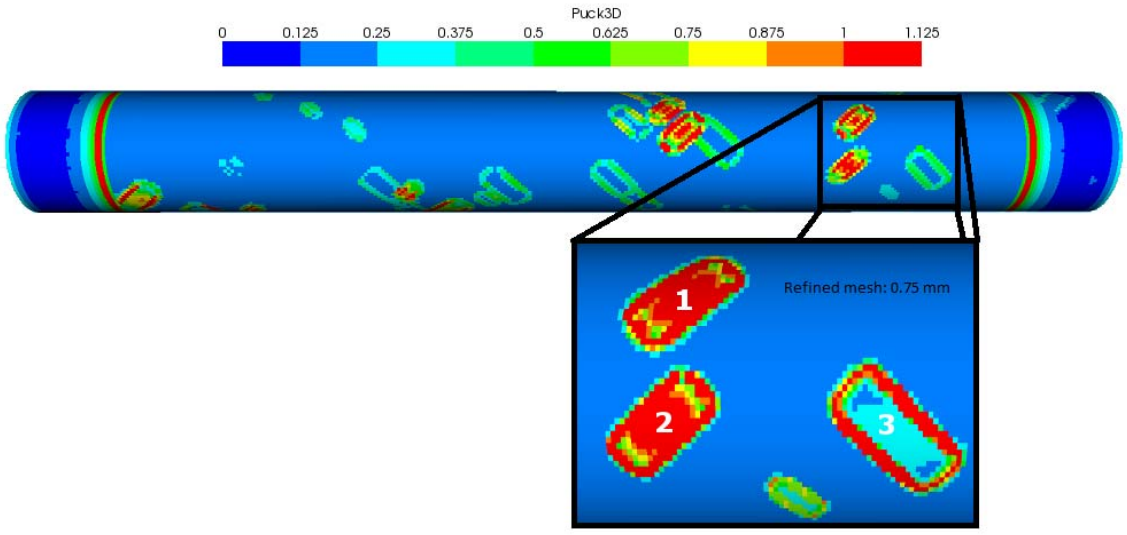

Figure 12: Element-wise maximum IRF of the Puck 3D failure criterion for a load of 1200 Nm. Three voids are highlighted in the box.

This effect was investigated further by consulting the through-the-thickness results of three individual, isolated voids highlighted within the box in Figure 12. *Void 1* is located in the -45°/+45° interface, *Void 2* is above the interface; *Void 3* is below the interface. The corresponding through thickness distribution of the IRF in the centre of each void is shown in Figure 13. The *void locations* are indicated by labelled rectangles and the –45°/+45° interface is marked with a dash-dotted line. *Void 3*, near the inner side of the laminate, has a much lower impact on the IRF when compared with *Voids 1* and *2*. The IRF only increases moderately close to the void and more at the adjacent plies inward from the void location. The failure mode however, does not change and the maximum IRF is still located in the ply just below the -45°/45° interface. In contrast, for both voids 1 and 2 the IRF increases significantly away from the void toward a maximum at the surface of 1.6. Also noteworthy is the change in the dominant failure mode from pmC at the interface, Figure 11, to pmA near the surface. The failure modes pmB (combined shear and compressive matrix failure) and pd (ply delamination) also occur but do not dominate the failure mechanism. The X-ray CT scan of cylinder B1 indicates that a void of relevant size is always found in the outer critical layer bundle. This explains the reduction of the limit load from 5900 to 1200 Nm when failure starts, and the change in failure mode to a tensile matrix failure explains the explosive growth of a matrix crack on the specimen surface.

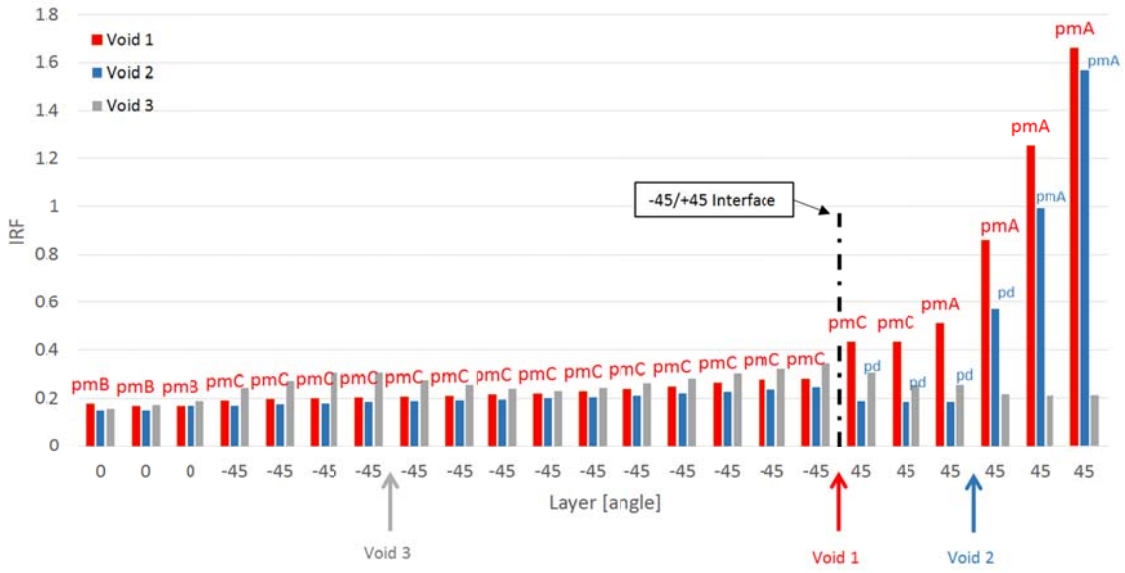

Figure 13: Through-the-thickness IRF distribution of Void 1 (red), Void 2 (blue) and Void 3 (grey) for VD1 and a torsional moment of 1200 Nm.

The same evaluations were repeated for VD2. Due to the smaller void size, a finer mesh was needed to obtain reliable results. The simulated external load was taken to be 1400 Nm in accordance with the measured limit loads of cylinders with peel ply finish B2, B4 and B5 of 1400, 1400 and 1500 Nm, respectively. A typical IRF distribution is shown in Figure 14. In this case, it is less obvious how the through-the-thickness distribution of the voids affects the strength. Due to the smaller size of the voids in VD2, the edge effects due to meshing are more prominent than in VD1.

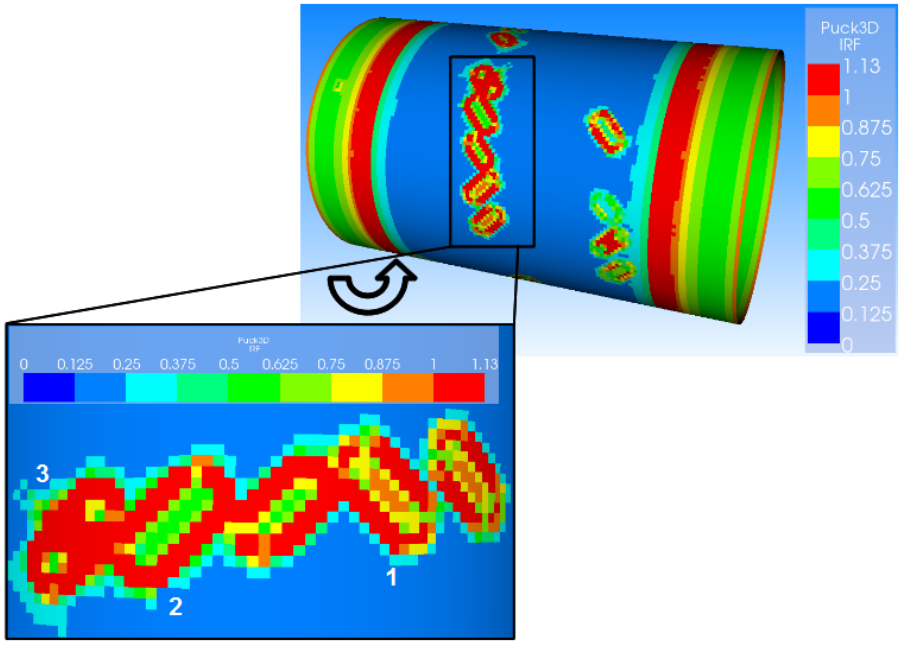

Figure 14: Global IRF distribution for a load of 1400 Nm and detail view of simulated void distribution VD2. Three Voids are high-lighted in the box.

The through-the-thickness distribution of the IRF (Figure 15) corresponding to *Voids 1* and *2* highlight again, that the IRF is critical if the void is above the -45/+45° interface, similar to what is observed in VD1. In this case, the maximum IRF is 1.0 and 0.5 for *Void 1* and *2*, respectively, and the failure mode distribution is similar to VD1, Figure 13, i.e. if the void is at or above the -45°/+45° interface, the critical failure mode is pmA, with IRF increasing towards the surface ply. *Void 3* in the distribution VD2 investigates the effect of stacking voids, one above (3a) and two below (3b and 3c) the critical interface, a typical situation that is also found in the CT data of specimen B6.

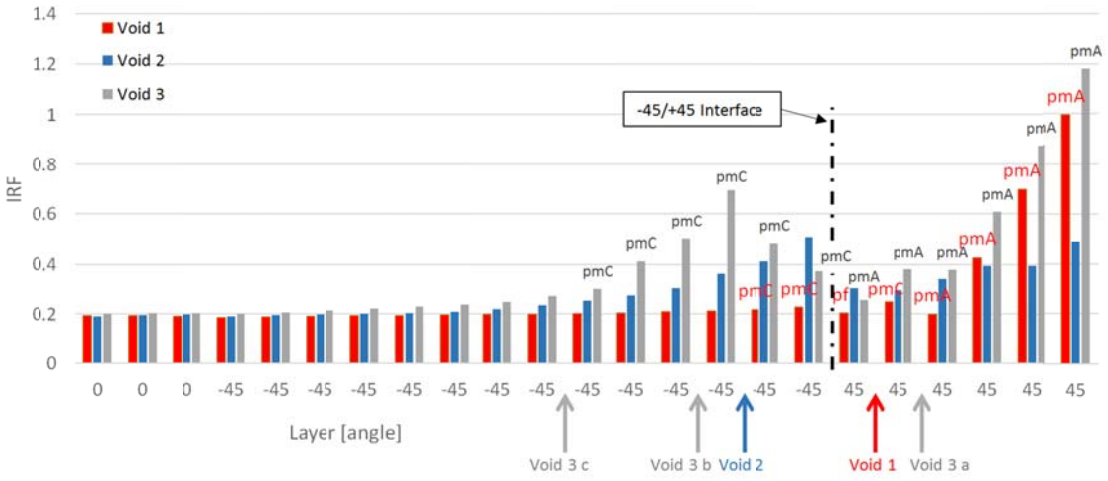

Figure 15: Through-the-thickness IRF distribution of Void 1 (red), Void 2 (blue) and stacked Voids 3a, b, c (grey) for void distribution VD2.

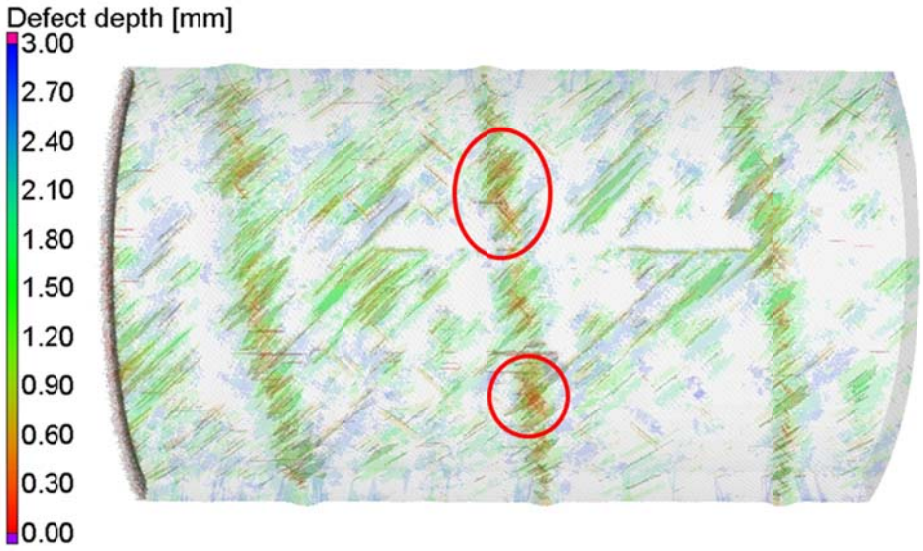

Figure 16: Defect depth distribution for sample B6.

Figure 16 shows the void content colour coded according to depth below the surface. The red rings highlight two regions with voids stacked in both the -45° and +45° plies. The proximity of Voids 3b and 3c leads to a greater combined effect on the local IRF compared to Void 2, despite Void 2 being closer to the interface. However, the IRF due to the combined Voids 3b and 3c still decreases towards the -45°/+45° interface to a value similar to the corresponding Void 3 in distribution VD1, Figure 13. Combining Void 3a has a similar effect on the IRF as Void 1. It causes the IRF to continuously increase

towards the surface ply and changes the dominant failure mode from pmC below the interface to pmA in the surface ply.

A parametric study of the influence of the void's area and position is shown in Figure 17. The surface chart shows the maximum IRF at the centre of a single void by varying its through-the-thickness position from layer interface 1 to the surface and its area from 66 to 500 mm^2. The loading is kept constant at 850 Nm. The IRF increases abruptly as soon as the void is in the -45°/+45° interface; whereas the effect of the area is much smaller. It can be concluded that the most critical feature of a void is its location within the laminate thickness, with a secondary influence coming from size and interaction of stacked voids. Since the X-ray CT scans of both specimens B1 and B6 reveal a significant number of near surface voids, it is to be expected that the failure load and failure mode should be similar for both smooth and rough cylinders, despite the significant difference in the number and size of voids resulting from the two manufacturing processes.

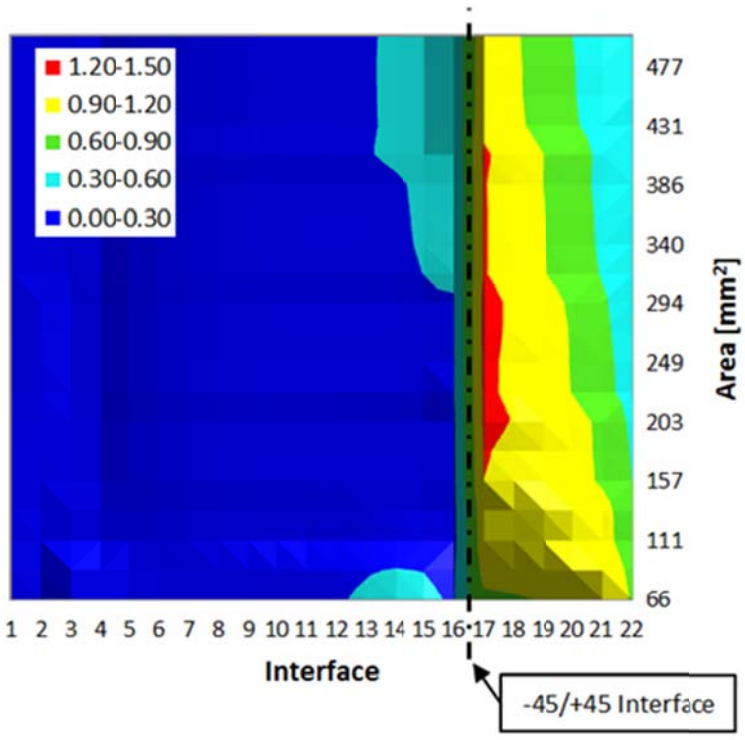

Figure 17: Maximum IRF vs void's position and area. Torsional load is 850 Nm.

Similar results were obtained when the torque was reversed, i.e. the outer fibres were loaded in compression. As expected, the FE simulation predicts a change of the dominant failure mode from pmA to pmC and vice versa for the +45° and -45° layers, respectively. Voids in the interface or one of the outer layers lead to an increase of the IRF towards the cylinder surface layer, as seen above for Voids 1 and 2, and a dominant pmC failure. Inclusion of a void in the inner layers such as Void 3 in VD1 or Void 3c in VD2 also increases IRF near the void. But the effect is much more pronounced under reversed loading and failure initiation is expected at the inner layer next to the void.

4.4 Estimating the TSA signal

The simulations of the surface stress distribution on top of the voids using the updated FE model allows for a calculation of the expected TSA response using typical material parameters. In Table 3 the surface stress components are given for a non-defective cylinder as well as for Void 1 and Void 2 of VD2, see Figure 14. Principal stress component σ_2 increases by a factor of 6 in the presence of voids. Since the Coefficient of Thermal Expansion transverse to the fibre direction is much larger than along the fibre, typically $26 \times 10^{-6}\ K^{-1}$ compared to $-0.3 \ldots -0.9 \times 10^{-6}\ K^{-1}$, an increase in the thermoelastic response of a factor of 2 to 5 is expected. Experimental data corroborate this finding. TSA values found for the non-defective areas of the cylinder are compared to areas with higher response in Table 3, see Figure 18 and Figure 19 below, revealing an increased TSA response by a factor of 5 to 7.

Table 3: Simulated surface stresses for a torsional load of 600 Nm and experimental thermoelastic responses for 200 Nm.

	σ_1 (FEA) [MPa]	σ_2 (FEA) [MPa]	ΔT (Exp) specimen B4 [K]	ΔT (Exp) specimen B1 [K]
non-defective area	-97.7	2.0	0.010 to 0.013 K	0.002 K
void 1 (VD2)	-76.0	12.5	0.05 to 0.10 K	0.012 to 0.015 K
void 2 (VD2)	-66.0	12.4		

4.5 Torsion tests on smooth surface specimens

An initial test was conducted using specimen B0 to verify that the inspection using TSA under torsional loading as described in section 3.3 could reveal defects. Figure 18 shows TSA amplitude images, each containing three views: the central direct view to the cylinder and two reflected views from the mirrors (above and below in these rotated views) showing the specimen from behind and to either side. The data obtained (Figure 18, top left) show that the majority of the specimen has a fairly low response (typical for CFRP) of the order of 0.004 °C. In a number of areas, the thermoelastic response is significantly greater (0.01 – 0.025°C) which confirms that defects have a clearly visible effect on the thermoelastic response under torsion. The large difference in the thermoelastic response between a defect free and void containing region provided confidence in using TSA to inspect the specimens prior to the static tests to failure. Two potential failure initiation sites were thus identified in specimen B0, circled in red in Figure 18, top left. The torsional load was increased in steps of 250 Nm and cycled at each level with amplitude of 100 Nm for TSA measurements. Failure occurred at 1000 Nm, slightly lower than the FEA predictions for model void distribution VD1. A comparison between the images before and after failure suggests that the failure initiated indeed from the region of increased thermoelastic response highlighted in Figure 18, top left. Furthermore, the failure manifested the explosive growth of a matrix crack in the surface ply and a corresponding delamination at the –45°/+45° interface.

The experiment was repeated with cylinder B1. The ΔT image in Figure 18, top right, shows the thermoelastic response of the pristine specimen again with signatures of near surface flaws which had been corroborated with CT and DSPI pre-test (see Figure 8). A *quasi*-static load ramp was then applied until a crack was initiated on the surface of the specimen at 1200 Nm. The crack initiated from the defect circled in red in Figure 18, top right. After crack initiation, the load was reduced again to 250 Nm and a delamination was grown by further cyclic loading with amplitude of 100 Nm. The grown defect is highlighted by red circles in Figure 18, bottom right. The TSA images were taken at a mean load of -250 Nm with amplitude of 100 Nm. Thus, the specimen was still able to support load, i.e. it was not completely failed. The extent of the damage in specimens B0 and B1 was assessed post-failure with close-up TSA in-situ and with DSPI in the laboratory, see section 4.7.

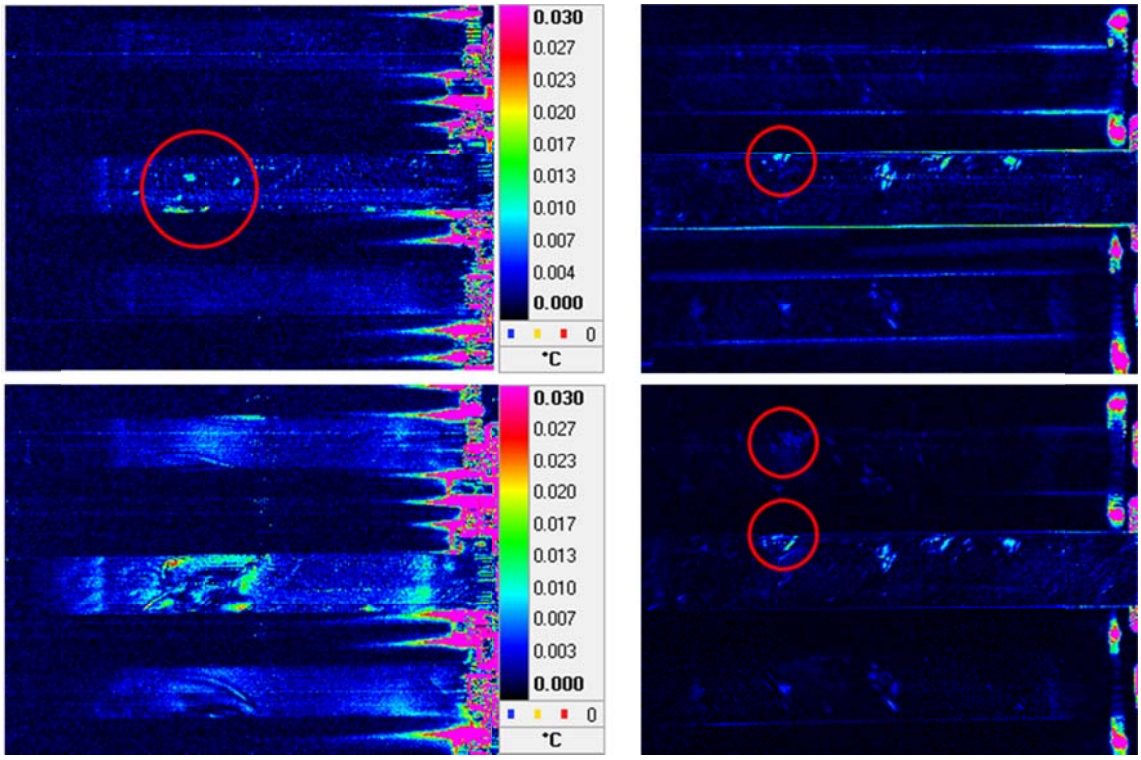

Figure 18: Left: TSA amplitude data, ΔT, from specimen B0 cyclically loaded at (-500±100) Nm and frequency 2 Hz, before (top left) and after failure (bottom left). Right: Specimen B1 before (top right) and after growth of debonding (bottom right), measured at (-250±100) Nm and frequency 2 Hz.

4.6 Torsion tests on rough surface specimens

Specimens B4 and B5 were inspected using TSA before testing. Stitched images of the thermoelastic temperature change (ΔT) such as the one shown in Figure 19 (specimen B4, face 4) show bands of increased thermoelastic response along the peel ply overlaps. This corresponds to regions with increased void counts observed in the X-ray CT data and the predicted increase in the thermoelastic response from the FEA. Failure would therefore be expected to originate from a region such as the band highlighted by the red oval in Figure 19.

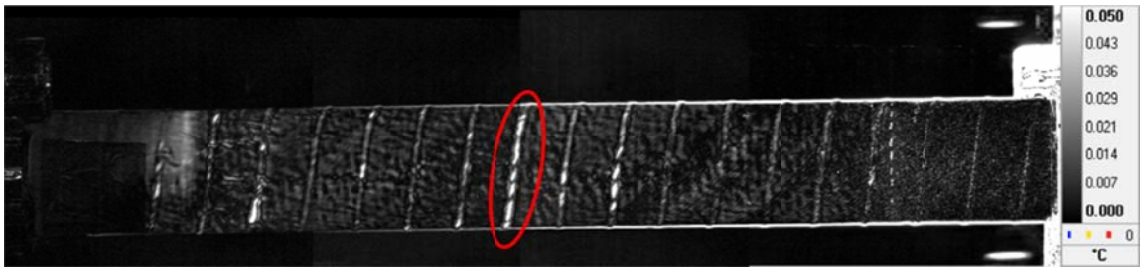

Figure 19: TSA amplitude data, ΔT, of specimen B4 showing bands of increased thermoelastic response along the peel ply overlaps.

Note that what appears to be noise in the TSA data are actually 45° striations associated with the fibre orientation in the surface ply, and fibre waviness commonly observed in UD carbon fibre laminates made from prepreg material.

Both specimens B4 and B5 were subsequently loaded to failure in a quasi-static test, failing at 1400 Nm and 1500 Nm, respectively. An IRT image of specimen B4 is shown in Figure 20. The image focuses on the face in the TSA data in Figure 19 because this had the highest thermoelastic response. Figure 20 is the first frame immediately after the failure has occurred and is taken from a video recorded at 383 Hz.

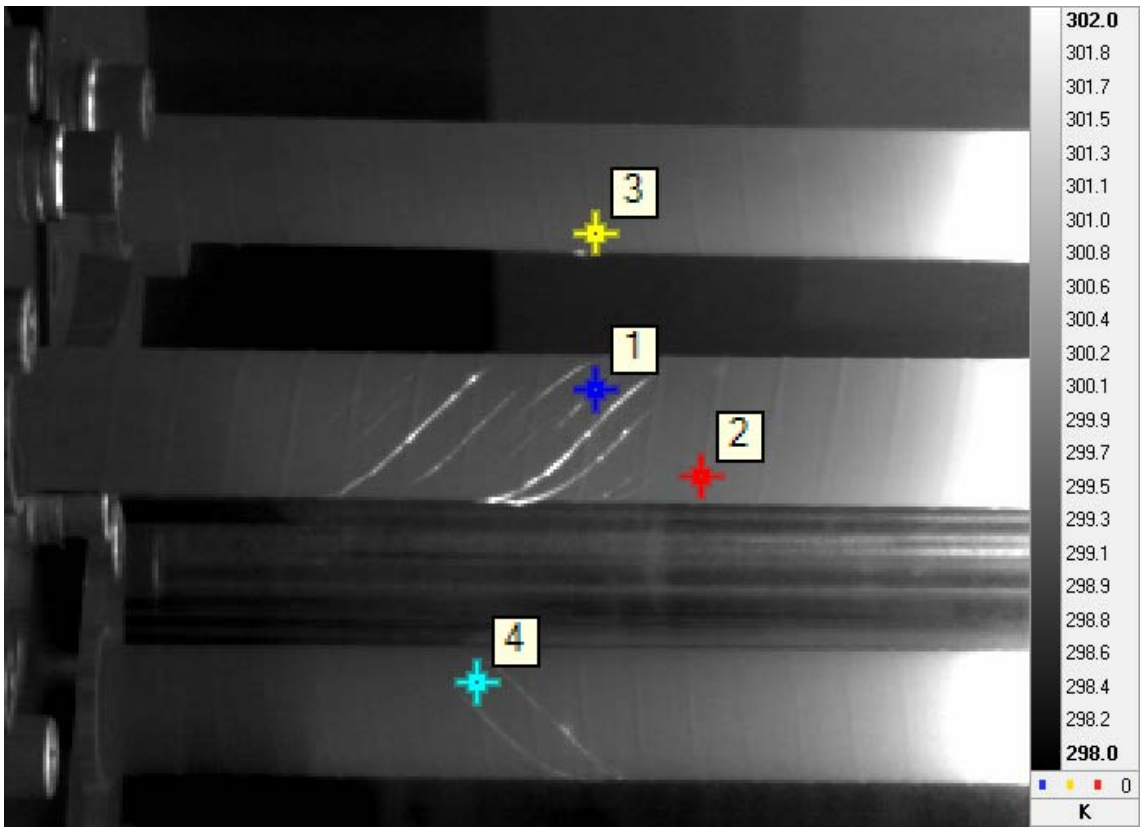

Figure 20: IRT image of specimen B4 showing the first frame after failure. The temperature increase at the newly formed crack surfaces is clearly visible. Points 1 – 4 highlight points where small cracks initiated before final failure.

Several matrix cracks can be seen on the surface, still 'hot' from the energy released during the sudden formation of the crack surfaces, i.e. 1-2 K warmer than the surrounding material. The marks 1 – 4 number points in order of appearance where a small temperature rise of the order of 0.1 to 0.2 K was registered prior to failure. This small temperature rise was due to the heat released during the formation of a crack and represents the onset of failure. A strong correlation is found between crack initiation and bands of high thermoelastic response that are associated with increased void density. Point 1, where the first of

these cracks formed, lies exactly on the line of increased thermoelastic response highlighted in Figure 19. Point 2, where the second crack formed, lies just next to a second such line of increased thermoelastic response. These initial cracks formed at a load of approximately 1300 Nm, 100 Nm before final failure. Final failure then occurred suddenly over a fairly large area that encompasses points 1 and 4. Points 2 and 3 were just beyond the limit of the main area of delamination which occurred in the -45°/+45° interface. This corresponds with the results from the FEA which showed both a change in failure mode and failure load resulting from the voids. The increase in thermoelastic surface response above a void was found to be 5 to 8 times greater than that of the surroundings in the experiment. In the simulation the response was found to be 3 to 5 times greater than the surroundings.. This may be explained by the slightly simplified geometry in the model, and the experiment containing several overlaid voids as opposed to single voids at different defect depths.

4.7 Post-failure assessment

After failure, cylinder B0 was subjected to low level loading using TSA to find the delamination boundaries with higher spatial resolution, along with comparative measurements obtained using DSPI. In Figure 21 four sectors are shown covering the full circumference of the cylinder at the damage location with the DSPI views slightly rotated and axially shifted w.r.t. the TSA images. The damage boundaries follow the +45° orientation of the fibres. While TSA mainly delineates the borders of the delamination as the stress is a maximum at those locations, DSPI shows the area more clearly due to the larger deformation of the debonded layers under thermal and mechanical load

For cylinder B1 the growth of one of the initial voids into a small delamination is evidenced in Figure 22. The through-the-thickness failure plots for the different voids show that the critical failure mode is matrix failure due to tension (pmA) if a void can be found in the outer layers, Figure 13. Assuming that this is the initial failure, it is probable that this defect propagates inwards as long as the fibre orientation does not change. At the -45°/45° interface the crack may stop, propagate further inwards or initiate a delamination. Failure modes at the interface may be of type pd and pmC which then further propagate and cause the large debonding/delamination as confirmed with DSPI. An X-ray CT scan of specimen B3 after failure is shown in Figure 23. The failure pattern indicates that matrix failure occurred in the outer layer bundle, stopped at the -45°/+45 interface, from where a large delamination is observed.

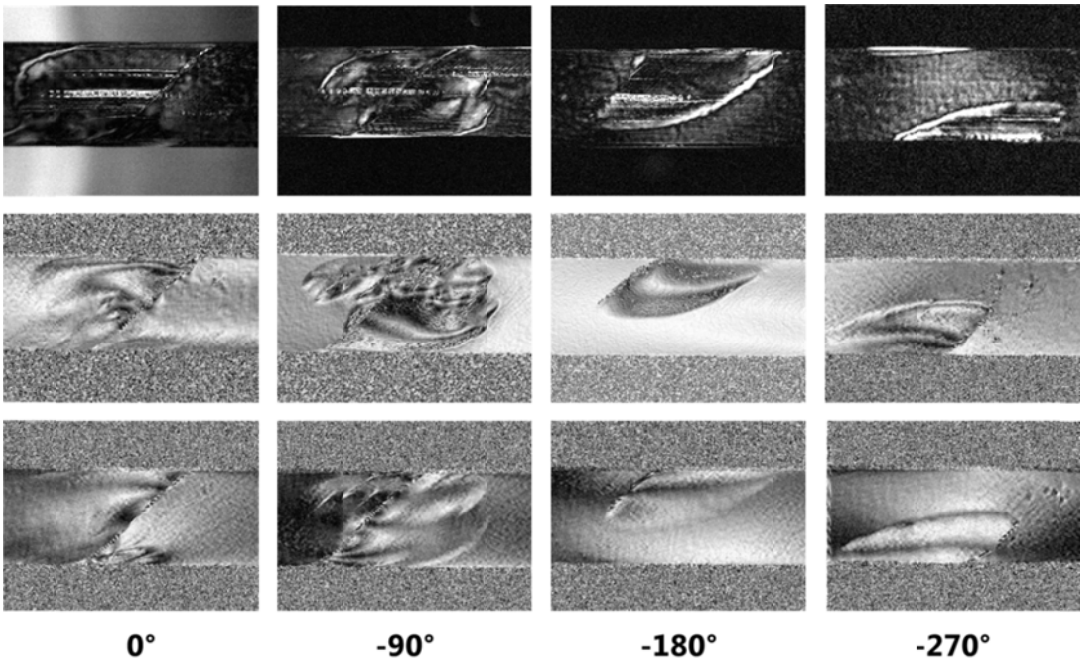

.

Figure 21: Assessment of the delaminated area in cylinder B0: Comparison of TSA amplitude data from torsional loading (top), DSPI phase gradient data from thermal loading (middle) and mechanical loading (bottom).

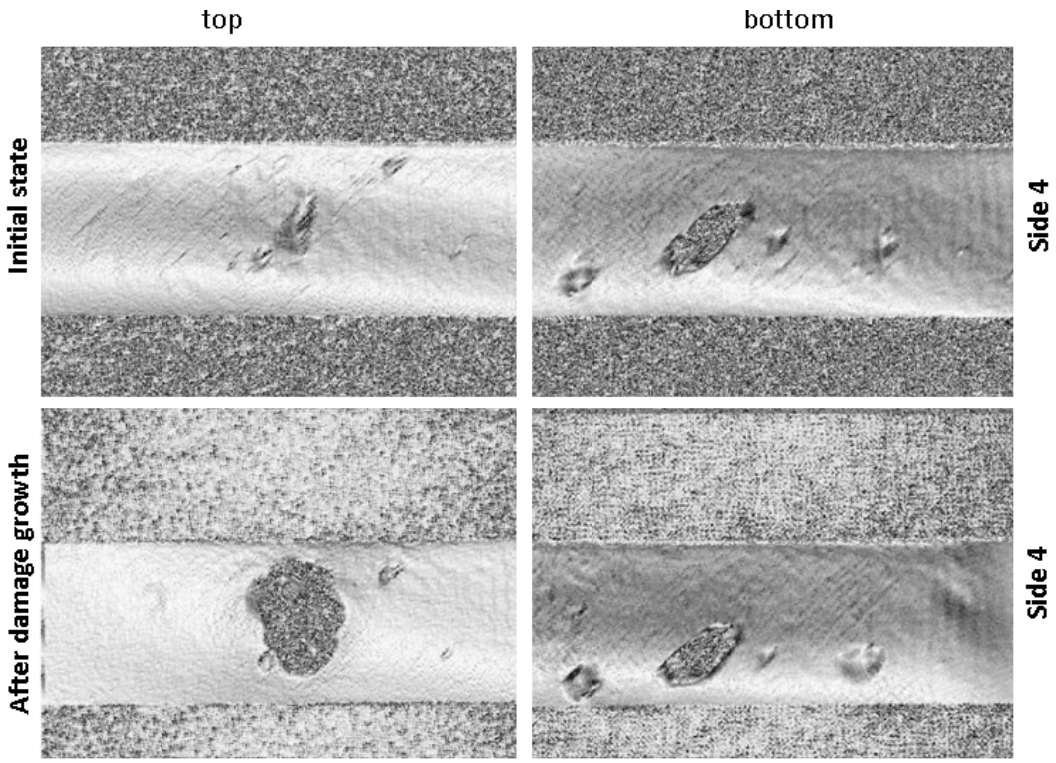

Figure 22: DSPI phase gradient images of cylinder B1 before testing (top) and after damage growth (bottom). Refer also to Figure 18 (right)

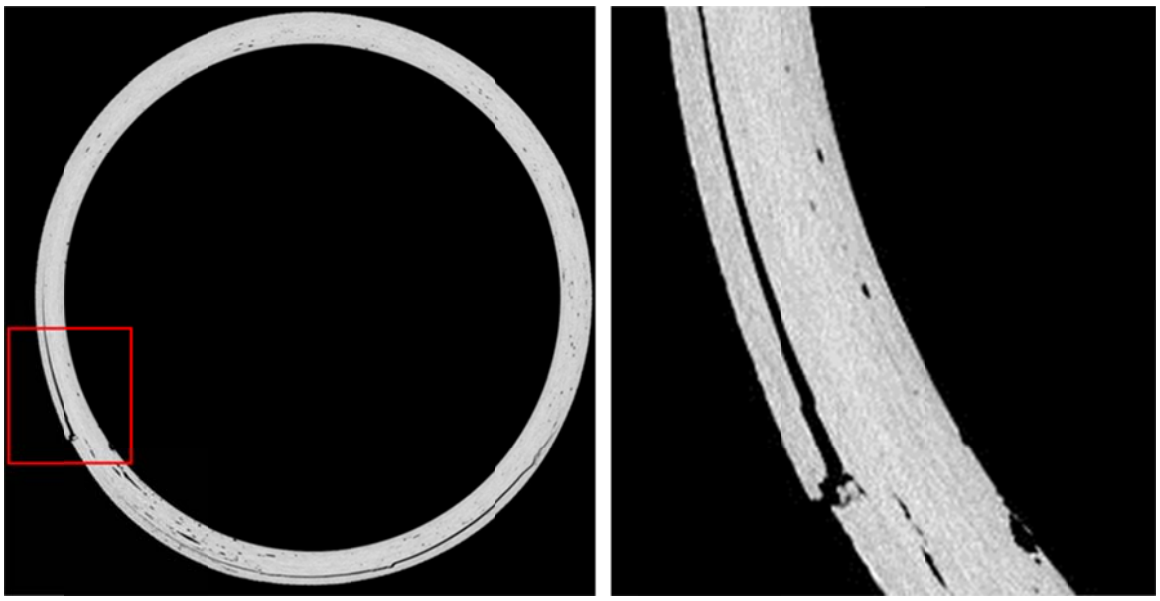

Figure 23: X-ray CT scan of specimen B3 after failure (left) and detail view of the delamination (right).

5. Discussion and Conclusions

The presence of major manufacturing flaws in CFRP torsion cylinders identified with X-ray CT are confirmed by indications of stress concentration in TSA data or inhomogeneities in deformation patterns obtained by DSPI. TSA is well-suited to obtain an in-process monitoring of the component under cyclic load, while DSPI can be used pre- and post-test to relate structural inhomogeneities to flaws and defects. FE simulations provide vital information of the criticality of the flaws that have been spotted by full-field techniques. They confirm that the presence of voids reduces ultimate strength while torsional stiffness is hardly affected. However, flaws do not uniquely relate to the damage initiation site mainly because of their number and randomness. Prediction of the first ply failure site is not possible except when a clear hierarchy of defect sizes and locations is available. The use of IRT to spot initial cracking during loading can indicate the critical sites and prevent catastrophic failure.

FE simulations suggest that the presence of voids changes the failure mode of an unflawed component. What in an ideal specimen would have been a pmC failure, due to the presence of imperfections, changes to a pmA failure. This demonstrates the importance of understanding the nature and distribution of defects in the selected manufacturing process; otherwise even the best failure models cannot correctly

predict either the failure mode or the failure load. A good agreement between measured and evaluated failure load (first ply failure) has been achieved. Furthermore, the data from FE simulation were used to estimate the temperature response in TSA measurements.

For the specific layup in the CFRP cylinders it has been shown that the failure load and failure mode are similar for both smooth and rough cylinders, despite the significant difference in the number and size of voids resulting from the two manufacturing processes. It can be concluded that the most critical location of a void is near the surface, with a secondary influence coming from size.

It was possible to grow a defect by applying torsion fatigue when considerable voids were already present in the specimen. While in specimen B1 a debonding was grown by cyclic torsional loading from an appreciable manufacturing flaw, small manufacturing voids in the peel-ply specimen B2 could not be grown by applying torsion. These voids led to catastrophic failure at loads well below those expected from an unflawed specimen.

Acknowledgements

Part of this work was performed within the MATERA+ project AMUSED [2]. Funding by the UK Technology Strategy Board under reference No. 620008 and the Swiss Commission for Technology and Innovation under contract No. 10701.3 PFIW-IW is gratefully acknowledged.

We thank the AMUSED partners Airbus (UK), GE Aviation, FLIR Systems Ltd, LaVision UK Ltd, AWE plc, and Carbo Link GmbH for their contributions to the AMUSED project. We thank Daniel Voelki from Empa Laboratory *Mechanical Systems Engineering* for operating the torsion test machine and Iwan Jerjen from the *Centre of X-ray Analytics* at Empa for his support with the CT-measurements.

References

1. Krause OK, C. Summary fatigue test report, OPTIMAT test report no. OB TG1 R026 rev. 0. 2006.

2. Matera-Project. AMUSED (Advanced MUlti-scale Strain basEd non-Destructive evaluation).

3. Soden PD, Kaddour AS, Hinton MJ. Recommendations for designers and researchers resulting from the world-wide failure exercise. Compos Sci Technol. 2004;64(3-4):589-604.

4. Avdelidis NP, Hawtin BC, Almond DP. Transient thermography in the assessment of defects of aircraft composites. Ndt&E Int. 2003;36(6):433-9.

5. Su ZQ, Ye L. Lamb wave-based quantitative identification of delamination in CF/EP composite structures using artificial neural algorithm. Compos Struct. 2004;66(1-4):627-37.

6. Leong M, Overgaard LCT, Thomsen OT, Lund E, Daniel IM. Investigation of failure mechanisms in GFRP sandwich structures with face sheet wrinkle defects used for wind turbine blades. Compos Struct. 2012;94(2):768-78.

7. Quaresimin M, Carraro PA. Damage initiation and evolution in glass/epoxy tubes subjected to combined tension-torsion fatigue loading. Int Journal of Fatigue. 2014.

8. Antoniou AE, Kensche C, Philippidis TP. Mechanical behavior of glass/epoxy tubes under combined static loading. Part I: Experimental. Compos Sci Technol. 2009;69(13):2241-7.

9. Antoniou AE, Kensche C, Philippidis TP. Mechanical behavior of glass/epoxy tubes under combined static loading. Part II: Validation of FEA progressive damage model. Compos Sci Technol. 2009;69(13):2248-55.

10. Puck A, Schurmann H. Failure analysis of FRP laminates by means of physically based phenomenological models. Compos Sci Technol. 2002;62(12-13):1633-62.

11. Kaddour AS, Hinton MJ, Smith PA, Li S. A comparison between the predictive capability of matrix cracking, damage and failure criteria for fibre reinforced composite laminates: Part A of the third world-wide failure exercise. J Compos Mater. 2013;47(20-21):2749-U147.

12. Kaddour AS, Hinton MJ. Maturity of 3D failure criteria for fibre-reinforced composites: Comparison between theories and experiments: Part B of WWFE-II. J Compos Mater. 2013;47(6-7):925-66.

13. Puck A, Schurmann H. Failure analysis of FRP laminates by means of physically based phenomenological models. Compos Sci Technol. 1998;58(7):1045-67.

14. Kroll L, Ehrlinspiel H, Czech A, Mueller S. Identification of Anisotropic Damage on CFRP Tubes Using Computer Tomography and Automated Analysis Methods. In: Proceedings of 17th International Conference on Composite Materials (ICCM17). Edinburgh, Conference, Conference 2009.

15. Feldkamp LA, Davis LC, Kress JW. Practical Cone-Beam Algorithm. J Opt Soc Am A. 1984;1(6):612-9.

Figure Captions

Figure 1: Puck matrix failures (reproduced from [10]).

Figure 2: Test sample B1 as manufactured with steel inserts for torsion testing (top), and sample B6 with peel ply finish (bottom).

Figure 3: Fibre orientation for 0°, –45°, +45° and the global coordinate system.

Figure 4: Model assembly - bonded contact of the steel inserts and CFRP cylinder.

Boundary conditions: fixed support on the left and torsional moment is applied on the right.

Figure 5: Test specimen mounted on the test machine with the two metal mirrors.

Figure 6: CT scans of a 110 mm section of cylinder B1 (top) and B6 (bottom) with colour coded defect volume. Note that the colour scale is different by a factor of 120 for the two specimens.

Figure 7: Void volume distribution of cylinder B1 (VD1, blue) and B6 (VD2, red).

Figure 8: Section of cylinder B1 with manufacturing flaws. CT-data colour coded for defect depth (top); DSPI phase gradient data (centre). TSA amplitude data with a slightly rotated view (bottom). The images are flipped in order to reproduce the orientation of the CT data.

Figure 9: Exemplary void distribution for VD1 (left) and VD2 (right).

Figure 10: Section cut of the final solid model with two highlighted voids.

Figure 11: Inverse reserve factors for each layer of a laminate without voids calculated for a torsional moment of 1200 Nm.

Figure 12: Element-wise maximum IRF of the Puck 3D failure criterion for a load of 1200 Nm. Three voids are highlighted in the box.

Figure 13: Through-the-thickness IRF distribution of Void 1 (red), Void 2 (blue) and Void 3 (grey) for VD1 and a torsional moment of 1200 Nm.

Figure 14: Global IRF distribution for a load of 1400 Nm and detail view of simulated void distribution VD2. Three Voids are high-lighted in the box.

Figure 15: Through-the-thickness IRF distribution of Void 1 (red), Void 2 (blue) and stacked Voids 3a, b, c (grey) for void distribution VD2.

Figure 16: Defect depth distribution for sample B6.

Figure 17: Maximum IRF vs void's position and area. Torsional load is 850 Nm.

Figure 18: Left: TSA amplitude data, ΔT, from specimen B0 cyclically loaded at (-500±100) Nm and frequency 2 Hz, before (top left) and after failure (bottom left). Right: Specimen B1 before (top right) and after growth of debonding (bottom right), measured at (-250±100) Nm and frequency 2 Hz.

Figure 19: TSA amplitude data, ΔT, of specimen B4 showing bands of increased thermoelastic response along the peel ply overlaps.

Figure 20: IRT image of specimen B4 showing the first frame after failure. The temperature increase at the newly formed crack surfaces is clearly visible. Points 1 – 4 highlight points where small cracks initiated before final failure.

Figure 21: Assessment of the delaminated area in cylinder B0: Comparison of TSA amplitude data from torsional loading (top), DSPI phase gradient data from thermal loading (middle) and mechanical loading (bottom).

Figure 22: DSPI phase gradient images of cylinder B1 before testing (top) and after damage growth (bottom). Refer also to Figure 18 (right)

Figure 23: X-ray CT scan of specimen B3 after failure (left) and detail view of the delamination (right).

Tables

Table 1: Material property values of the steel inserts and the carbon unidirectional (UD) prepreg used in the FEA. Parameter definitions are found in ref [13].

Structural Steel	E = 200.0 GPa	ν= 0.30	
Carbon UD prepreg	Orthotropic Elasticity		
	E_1 = 123.34 GPa	ν_{12} = 0.27	G_{12} = 5.00 GPa
	E_2 = 7.78 GPa	ν_{13} = 0.27	G_{13} = 5.00 GPa
	E_3 = 7.78 GPa	ν_{23} = 0.42	G_{23} = 3.08 GPa
	Orthotropic Stress Limits [MPa] [1]		
	X_T = 2600	Y_T = 34	Z_T = 34
	X_C = -1300	Y_C = -68	Z_C = -68
	S_{12} = 80	S_{13} = 80	S_{23} = 55
	Puck Constants [dimensionless]		
	$p_{\perp\parallel}^{(+)}$ = 0.35	$p_{\perp\parallel}^{(-)}$ = 0.30	
	$p_{\perp\perp}^{(+)}$ = 0.30	$p_{\perp\perp}^{(-)}$ = 0.25	
	Degradation factor M = 0.5	Degradation factor s = η = 0.5	Interface weakening factor f_w = 0.8

[1] **For unidirectional prepreg, X and Y correspond to the failure stresses in the principal material directions (i.e. 1 and 2). S is the failure shear stress. The subscripts T and C stand for tension and compression, respectively.**

Table 2: Test specimens, surface finish, torsion tests and measurements performed.

No	Finish	Torsion tests	IRT	TSA	DSPI	CT scan
B0	smooth	Quasi-static load to 1000 Nm	-	-	post failure	-
B1	smooth	Quasi-static load to 1200 Nm Cyclic load, defect grown by fatigue cycling	-	pristine and after defect growth	pristine and after defect growth	pristine
B2	peel-ply	fatigued to 80000 cycles Quasi-static test to failure 1400 Nm	during failure event	Every 1500 cycles	pristine	-
B3	peel-ply	Quasi-static test to failure 1300 Nm	during failure event	pristine	post failure	post failure
B4	peel-ply	Quasi-static test to failure 1400 Nm	during failure event	pristine	pristine	-
B5	peel-ply	Quasi-static test to failure 1500 Nm	during failure event	pristine	pristine	-
B6	peel-ply	not loaded	-	-	pristine	pristine

Table 3: Simulated surface stresses for a torsional load of 600 Nm and experimental thermoelastic responses for 200 Nm.

	σ_1 (FEA) [MPa]	σ_2 (FEA) [MPa]	ΔT (Exp) specimen B4 [K]	ΔT (Exp) specimen B1 [K]
non-defective area	-97.7	2.0	0.010 to 0.013 K	0.002 K
void 1 (VD2)	-76.0	12.5	0.05 to 0.10 K	0.012 to 0.015 K
void 2 (VD2)	-66.0	12.4		